JOURNAL OF MAGNETIC RESONANCE **131,** 327–335 (1998)
ARTICLE NO. MN981358

Pore-Structure Determinations of Silica Aerogels by ^{129}Xe NMR Spectroscopy and Imaging[1]

D. M. Gregory, R. E. Gerald II, and R. E. Botto[2]

Argonne National Laboratory, Chemistry Division, 9700 South Cass Avenue, Argonne, Illinois 60439-4828

Received August 25, 1997

Silica aerogels represent a new class of open-pore materials with pore dimensions on a scale of tens of nanometers, and are thus classified as mesoporous materials. In this work, we show that the combination of NMR spectroscopy and chemical-shift selective magnetic resonance imaging (MRI) can resolve some of the important aspects of the structure of silica aerogels. The use of xenon as a gaseous probe in combination with spatially resolved NMR techniques is demonstrated to be a powerful, new approach for characterizing the average pore structure and steady-state spatial distributions of xenon atoms in different physicochemical environments. Furthermore, dynamic NMR magnetization transfer experiments and pulsed-field gradient (PFG) measurements have been used to characterize exchange processes and diffusive motion of xenon in samples at equilibrium. In particular, this new NMR approach offers unique information and insights into the nanoscopic pore structure and microscopic morphology of aerogels and the dynamical behavior of occluded adsorbates. MRI provides spatially resolved information on the nature of the flaw regions found in these materials. Pseudo-first-order rate constants for magnetization transfer among the bulk and occluded xenon phases indicate xenon-exchange rate constants on the order of 1 s^{-1} for specimens having volumes of 0.03 cm^3. PFG diffusion measurements show evidence of anisotropic diffusion for xenon occluded within aerogels, with nominal self-diffusivity coefficients on the order of $D = 10^{-3}$ cm^2/s.

INTRODUCTION

Aerogels represent a new class of open-pore materials with pore dimensions in the nanometer range, typically between 2 and 50 nm, and are thus classified as mesoporous materials. Silica aerogels exhibit many unusual properties, including extremely low densities (0.003–0.35 g/cm^2), high thermal resistance, low refractive index and sound velocity, and high surface area. These unique properties allow for their use in many new applications, such as insulated windows for solar applications, catalysts, gas separation media, and Cherenkov counters (*1–5*). Silica aerogels have been synthesized using conventional sol–gel processing techniques from an ''alcogel'' precursor followed by supercritical solvent extraction, which leaves the original gel structure virtually intact (*6, 7*). Understanding the processes that control the pore structure is paramount to developing better approaches for producing more uniform microstructured materials.

Numerous techniques have been used to study the pore structure of silica aerogels. These materials have been difficult to characterize with certainty, largely because available measurement techniques for determining porosity characteristics can give drastically differing results on the same sample. The volume of gas adsorption determined by the method of Brunauer, Emmit, and Teller (BET) has been used to determine specific surface areas of aerogels, and the hysteresis in the adsorption/desorption curves has provided pore-size distributions via the Kelvin equation (*8–11*). While BET measurements have generally been valid in the determination of voids in the mesopore regime, there are significant limitations associated with the use of conventional gas adsorption methods to evaluate the total porosity of aerogels (*12*). It has been assumed that inconsistencies in the data result from the inability of BET measurements to adequately detect the micro- and macropore voids in these systems (*13*).

Mercury porosimetry has also been used in certain instances, but is not generally applicable to fragile aerogel networks, because the high compressive forces associated with the method can cause structural collapse (*14–16*). X-ray and neutron scattering techniques are particularly well suited for determining the fractal geometry of the pore network (*17*). Other methods such as electron microscopy and atomic force microscopy have had limited success in determining the pore network structure of aerogels to date.

Limitations of the various techniques used in the determination of porosity characteristics of aerogels has left several important aspects concerning their structure unresolved. Apparently, BET gas adsorption measurements do not account for the entire pore volume estimated from fractal analysis

[1] Work supported by the U.S. Department of Energy, Division of Chemical Sciences, Office of Basic Energy Sciences, under Contract W-31-109-Eng-38. The U.S. Government's right to retain a nonexclusive royalty-free license in and to the copyright covering this paper, for governmental purposes, is acknowledged.

[2] To whom correspondence should be addressed.

1090-7807/98 $25.00

(*17*). Does the volume which seems to be unaccounted for in BET measurements result from the inability of the method to detect the micro- and macroporosity in these systems, or rather does it reflect on the complete ''openness'' of the aerogel pore network?

Over the past two decades, ^{129}Xe NMR has become a popular technique for investigating the microscopic properties of porous materials (*18, 19*). The xenon atom has a large, polarizable electron cloud that is very sensitive to its local physical environment, and transmission of the effects to the xenon nucleus is largely responsible for the large range of ^{129}Xe chemical shifts. Previous studies have related bulk NMR properties of adsorbed xenon gas, primarily the xenon chemical shifts, to the physical structure properties of numerous microporous materials (*20–24*).

In this paper, we report the first direct evidence linking xenon chemical shifts to xenon occluded within a microporous system. We show that the combination of NMR spectroscopy and chemical-shift selective magnetic resonance imaging (MRI) can be used to resolve some of the important aspects regarding the structure of silica aerogels. The use of xenon as an imaging probe is shown to be a new promising tool for characterizing the pore structure of aerogels, and to evaluate steady-state spatial distributions of xenon atoms in different physicochemical environments. Moreover, dynamic NMR and pulsed-field gradient (PFG) diffusion measurements have been employed to characterize the mobility and diffusive motion of xenon in samples at equilibrium. Spatially resolved NMR methods offer unique information and insights into the nanoscopic pore structure and microscopic morphology of aerogels, as well as the dynamical behavior of occluded atomic and molecular adsorbates.

EXPERIMENT AND METHODS

Ampules for NMR investigations were prepared in the following manner. Three different specimens of silica aerogel (nominal dimensions: $3 \times 3 \times 3$ mm) were placed in a heavy-wall borosilicate glass sample tube (i.d. = 5.0 mm, o.d. = 9.0 mm, and length = 41 mm). The sample tube was evacuated and then the bottom of the tube was immersed in liquid nitrogen. An amount of xenon gas was allowed to enter the tube to create a pressure of 30 atm when the sample was allowed to warm to room temperature. The tube was then flame sealed. Prior to seal-off under liquid nitrogen, a small amount of relaxation agent (O_2 gas) was added to enhance the spin–lattice relaxation rate of occluded- and gas-phase ^{129}Xe nuclei.

NMR spectroscopy and chemical-shift imaging experiments were performed at a field of 9.4 T on a Tecmag Libra system, which was interfaced to a Bruker Instruments three-axis, shielded imaging probe and BR-40 gradient amplifiers. At this field, xenon nuclei resonate at a frequency of 110.8 MHz. Ampules with a nominal length of 30 mm were placed in a home-built solenoid coil having a diameter of 9 mm and a length of 20 mm. The coil geometry was designed to optimize both the filling factor and the fraction of the total signal due to occluded xenon. Care was taken to insure that all of the aerogel specimens were located inside the coil.

A 90° pulse width of 10 μs was employed in all experiments. Spin–spin relaxation time (T_2) measurements were performed using the standard Hahn spin-echo method (*25*). Spin–lattice relaxation times (T_1 values) were measured using the inversion-recovery method (*26*). The diffusion coefficients were measured using the APGSTE sequence of Lucas *et al.* (*27*). Gradient strengths ranged from 0 to 20 G/cm in 1.54 G/cm increments. The other APGSTE parameters were $\delta = 0.6$ ms, $\Delta = 50$ ms, $\tau = 0.8$ ms, $t_1 = t_2 = 0.1$ ms. The diffusion coefficients were found by fitting the integrated peak intensities to

$$A = A_o \exp[-\gamma^2 D(P\mathbf{g}_a^2)], \qquad [1]$$

where γ is the magnetogyric ratio of the observed nucleus, D is the local apparent diffusion coefficient, $\mathbf{g}_a$ is the local applied gradient strength, P is a function of the acquisition sequence timing parameters, and A_o is the equilibrium magnetization generated in the absence of diffusion-encoding gradients.

In order to measure the chemical shifts of the occluded xenon at lower pressures, several aerogel samples were placed inside a 10-mm NMR tube. The tube was sealed with a Young valve, at total gas pressures ranging from 100 to 1500 Torr. In all cases 50 Torr of O_2 gas was introduced as a relaxation agent. The 90° pulse width for the 10-mm diameter Helmholtz coil was 12 μs.

Chemical-shift selective imaging was accomplished using the SECSI method of Gerald *et al.* (*28*). The selection sequence is $90^\circ_X - \tau_{CH} - 90^\circ_{-X} - \tau_{null} - 90^\circ -$Image. The resonance(s) of the spin(s) to be imaged is placed at (or near) resonance. Because T_1 relaxation times of the three xenon resonances in the sample were similar, it was possible to suppress two resonances simultaneously; this was accomplished by implementing the SECSI sequence in the appropriate fashion, as described below. The τ_{null} times used in the experiments ranged from 0.7 to 0.9 s, and the recycle delay time used was 5 s. Images of either occluded or free xenon gas were obtained by setting the value of $\tau_{CH} = 150$ μs in the experiment. Selected images of the individual resonances of occluded xenon, at 52 and 47 ppm, were obtained with values of $\tau_{CH} = 910$ and 1030 μs, respectively. After chemical-shift selection was achieved using the SECSI filter, conventional 2D spin-echo imaging (*29*) was carried out using 64 phase-encoding steps; each step required 200–600 transients in order to obtain an adequate S/N ratio. The time to echo $\tau_E = 3.8$ ms. The in-plane pixel resolution was 420×420 μm. Slice selection was accomplished by

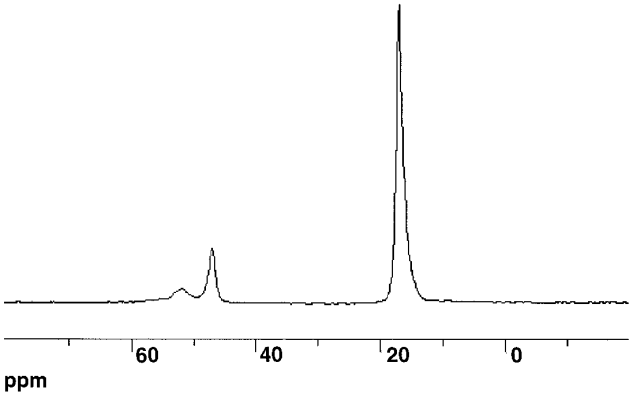

FIG. 1. ^{129}Xe NMR spectrum of the high-pressure sample (30 atm. of xenon); 64 scans were averaged. The chemical-shift reference is set to 0 ppm, which is the value of xenon gas extrapolated to zero pressure.

substituting a three-lobe, sinc 90° pulse in place of the third hard 90° pulse in the SECSI sequence. Slices were taken perpendicular to the main field axis of the superconducting magnet.

Magnetization transfer experiments were performed using a simple pulse sequence comprised of three sequential 90° pulses, analogous to the SECSI sequence described above. Following the second 90° pulse, magnetization vectors of spin ensembles with differing frequencies become aligned antiparallel along the direction of the *z* axis. The variable delay period following the second 90° pulse allows transfer of spin magnetization; a third 90° readout pulse was used to record the signal.

RESULTS AND DISCUSSION

The ^{129}Xe NMR spectrum of a high pressure sample containing xenon gas at a pressure of 30 atm is shown in Fig. 1. The chemical-shift reference of $\delta = 0$ ppm corresponds to the shift of pure xenon gas extrapolated to zero concentration. The resonance observed at 17 ppm is that of free (or bulk-phase) xenon gas in the sample tube, while the two smaller resonances arise from xenon occluded within the pores of the aerogel specimens. As we will see later in the NMR imaging experiments, resonances at 46 and 52 ppm can be assigned to optically transparent and translucent regions of aerogel specimens, respectively.

The ^{129}Xe spin–lattice relaxation times (T_1 values) and spin–spin relaxation times (T_2 values) for the three xenon resonances are reported in Table 1. No downfield resonances (between 120 and 230 ppm) were detected, which suggests that either the aerogels have little or no micropore structure, or that many xenon atoms found within a small fraction of micropores are in rapid exchange with those in larger pore domains. The spin–lattice relaxation times obtained are more difficult to interpret, because O_2 gas was introduced into the samples as relaxation enhancement agent. They were measured, however, to determine the τ_{null} value to be used in the SECSI experiments.

PFG diffusion measurements were repeated three times in each gradient direction. The *x* gradient is aligned along the direction of the long axis of the sample tube, and the *z* gradient is aligned along the direction of the superconducting magnetic field axis. The data are also summarized in Table 1.

Diffusion of xenon within aerogels is found to be about two times slower than diffusion of free xenon gas. This result is to be expected for xenon that is confined within a mesoporous material. Diffusion coefficients measured by the PFG method are the same in all three directions for both free gas and occluded xenon at $\delta = 52$ ppm, within an experimental error of ± 0.1 cm^2/s. On the other hand, diffusion coefficients measured for the resonance at 46 ppm, which corresponds to transparent regions in aerogels on the basis of the imaging results (vide infra), are slightly larger along the direction of the *y* gradient axis. The reason for the observed anisotropy is uncertain; however, it is possible that some degree of local ordering of the pore network structure had occurred as a result of gravitational forces during sample preparation. No attempt, however, was made to correlate the observed anisotropy in diffusion with orientation effects during preparation of the aerogels, since no prior sample history was documented. Therefore, we can simply conclude that spatial anisotropy in the xenon diffusion coefficients is observed, and that this may reflect an asymmetry in the pore structure of the transparent regions in aerogels. Whether this effect is a direct consequence of preparation conditions and whose origin is gravitational in nature warrants further investigation.

TABLE 1
^{129}Xe NMR Parameters Obtained for Silica Aerogels

	T_1 (s)	T_2 (ms)	D_C (*x* gradient)[a]	D_C (*y* gradient)	D_C (*z* gradient)
Free gas (17 ppm)	1.6	40	1.7×10^{-3}	1.7×10^{-3}	1.6×10^{-3}
Adsorbed (46 ppm)	1.2	10.9	1.1×10^{-3}	1.4×10^{-3}	1.2×10^{-3}
Adsorbed (52 ppm)	1.4	4.9	1.2×10^{-3}	1.2×10^{-3}	1.1×10^{-3}

[a] The diffusion coefficients are reported as cm^2/s; experimental error is $\pm 0.1 \times 10^{-3}$ cm^2/s.

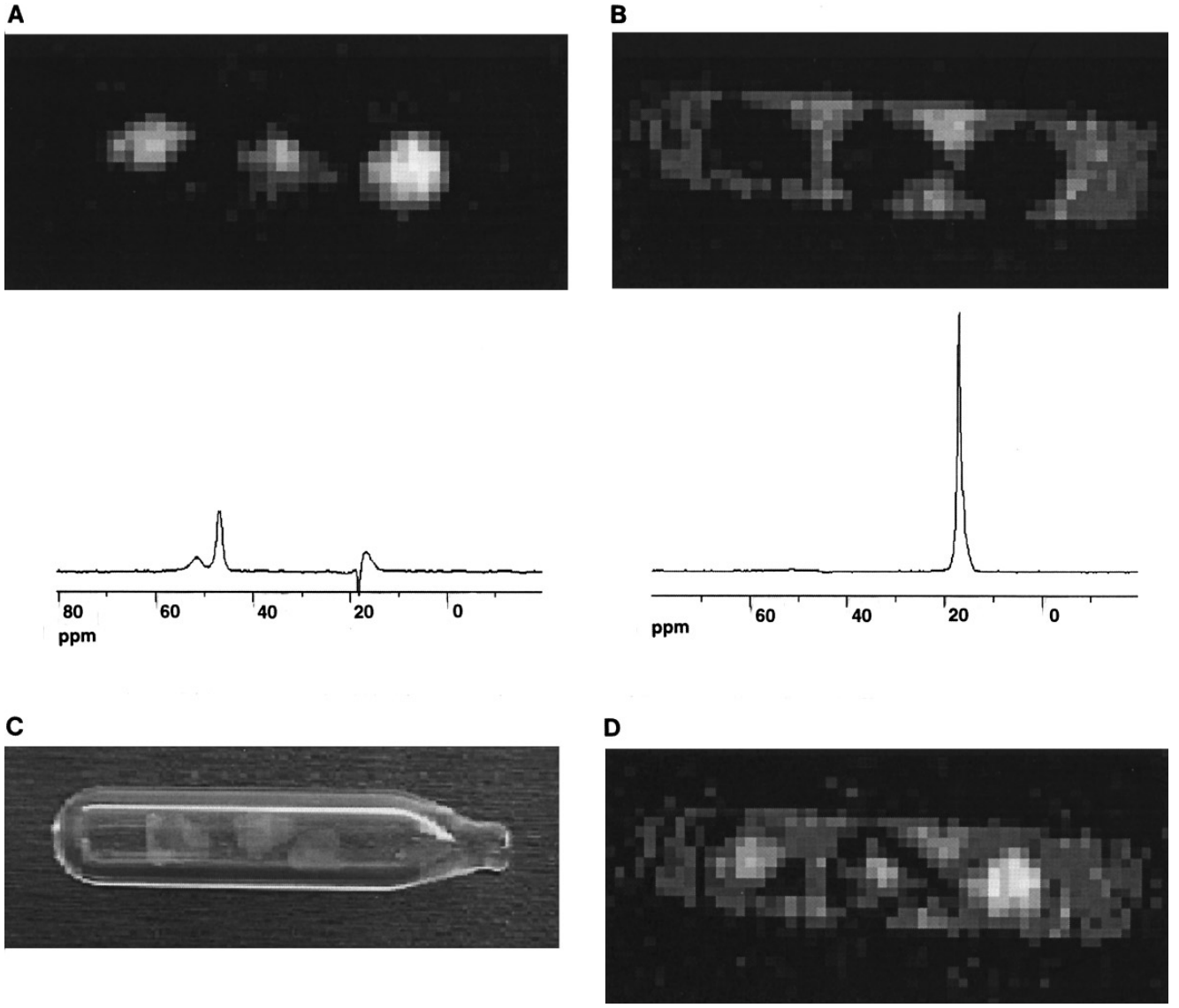

FIG. 2. Slices (1 mm in thickness) of ^{129}Xe chemical-shift selective NMR images. Brighter pixels indicate greater signal intensity. Below each image is a spectrum acquired with the identical chemical-shift selection sequence used to record the image. (A) Image of the xenon adsorbed inside aerogel specimens, in which the signal from the larger peak at 17 ppm has been suppressed. The spectrometer frequency was set to the resonance at 46 ppm. (B) Image of the xenon gas outside the aerogel samples, in which the signal from the resonances at 46 and 52 ppm has been suppressed. In this case, the spectrometer frequency was set to the resonance at 17 ppm. (C) Photograph of the high pressure sample showing the three aerogel samples. Translucent regions appear brighter in the photograph; transparent regions appear dimmer. (D) Image showing the direct addition of the data shown in (A) and (B). Signal intensity can be compared directly pixel by pixel. Black regions depict areas where there is apparently no detectable signal (the signal intensity is below the noise threshold).

NMR Imaging

^{129}Xe chemical-shift imaging provides the first conclusive evidence of the direct correlation between δ_{Xe} and the location of xenon within aerogel samples. Figure 2 shows ^{129}Xe imaging results for the high-pressure xenon/aerogel sample. Slices of SECSI images of occluded and bulk-phase xenon gas are shown in Figs. 2A and 2B, respectively. Chemical-shift selected spectra are shown directly below each of their respective images. A photograph of the three aerogel specimens sealed inside the high-pressure ampule is shown in Fig. 2C for comparison.

Visual inspection of the chemical-shift selective images obtained by the SECSI pulse sequence clearly demonstrates the effectiveness of the method for isolating distinct reservoirs of bulk-phase (free) and occluded xenon in the specimens. Comparing the photograph with the NMR image of occluded xenon clearly reveals a general overall correspondence between internal structural features and specimen morphologies. It is apparent from viewing the images that

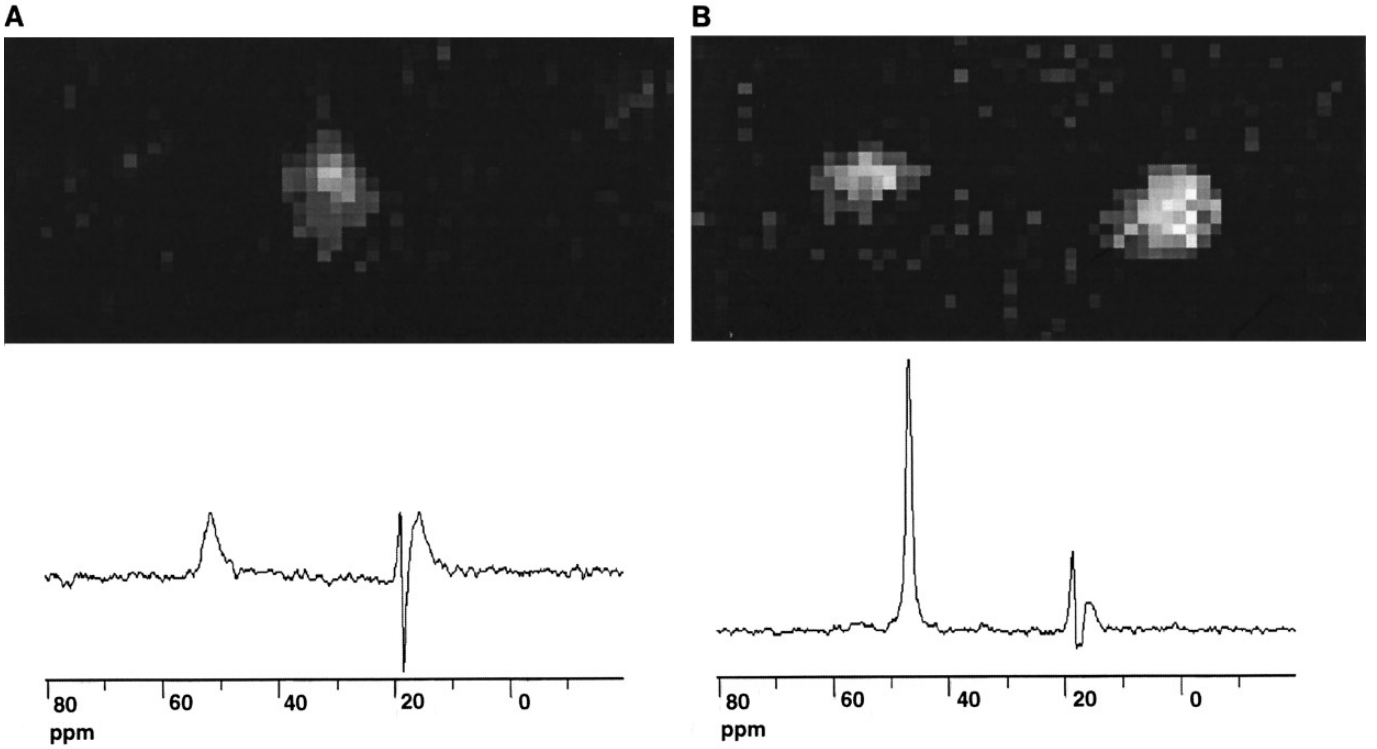

FIG. 3. Slices (1 mm in thickness) of ^{129}Xe chemical-shift selective NMR images. (A) Signal from the resonance at 52 ppm has been selected while the other resonances have been suppressed. (B) Signal from the resonance at 46 ppm has been selected.

the adsorption properties of xenon are very different in the three specimens. For instance, the middle image appears to be smaller and is considerably less intense than the image directly to its right, even though the two physical specimens are comparable in size. Also, the concentration of xenon is greatest in the center of the right image; xenon intensity diminishes progressively toward its outer edges. Signal intensity in the left image appears to be intermediate to those of the other two specimens, and the size of the image appears to be smaller than the actual specimen would suggest.

Figure 2D represents the composite image from both experiments, in which Figs. 2A and 2B have been added together. The sum of the two images allows a direct comparison of signal intensity of both bulk-phase and occluded xenon. The most striking feature seen in the composite image is that entire regions devoid of xenon signal can be identified; in particular, regions are evident at the edges of images at the left and middle of the figure. Moreover, the total concentration of xenon in the specimen at the right is significantly greater than the concentration of xenon in the surrounding free gas; the concentration of occluded xenon is found to be nearly twice the concentration of xenon in the bulk phase.

The ability to suppress two xenon resonances simultaneously in the imaging experiment makes it possible to image either of the two occluded xenon resonance lines independently. The ^{129}Xe chemical-shift selective images utilizing this protocol are depicted in Fig. 3. Figure 3A clearly demonstrates that xenon having a chemical shift of $\delta = 52$ ppm resides within the middle specimen exclusively. On the other hand, Fig. 3B shows that xenon at $\delta = 47$ ppm is present in the other two aerogel specimens. This spectroscopic information has important implications about the pore structure of aerogel networks, and clearly illustrates that the two xenon chemical shifts are associated with entirely different pore structures.

The images presented in Figs. 2 and 3 illustrate the ability of the xenon MRI method to study heterogeneity associated with the pore structure of aerogels. The most exciting aspect of this work is the power of xenon chemical-shift imaging for elucidating differences in the physical properties of aerogels. In particular, we have been able to correlate MRI results with optical properties of the specimens. Three distinct regions in the specimens can be clearly distinguished on the basis of differences in the xenon NMR parameters, and imaging facilitates their visualization. Recall that the middle specimen appears translucent, while the other two specimens are largely transparent, and that the specimen on the left has translucent regions at two of its outer edges (see Fig. 2C). Adsorbed xenon in the middle, uniformly translucent specimen is found to resonate at a higher frequency, and exhibits a broader resonance than xenon adsorbed in the other two

specimens, and thus is readily distinguished in the image depicted in Fig. 3A. The images highlighted in Fig. 3B for the outer two specimens constitute a second type of pore structure associated with optical transparency. A third pore regime can be ascribed to regions that are devoid of xenon signal, which occur at the edges of the center and left images, see Fig. 2D. These regions may have resulted from physical damage to the fragile aerogel specimens. They apparently are regions inaccessible to xenon and are consistent with a collapsed pore network.

A direct comparison of the overall image intensities of xenon in the aerogel specimens with that in the bulk phase is shown in the composite image, Fig. 2D. While image pixel intensities of bulk-phase xenon are relatively uniform throughout the 1-mm slice shown, the corresponding intensity variation of xenon occluded within specimens is significantly more pronounced. The specific loss of signal intensity near the edges of specimens may, in part, be attributable to exchange between xenon atoms in occluded and bulk phases, which is likely to occur to a significant extent during the pulse delay periods in the imaging experiment. The appearance of a symmetrical dark halo around the edge of the bright image (found at the right of Fig. 2D) is consistent with the foregoing argument; however, the topic of xenon-atom exchange will be discussed in greater detail later.

Perhaps a more significant finding is that dark regions are not uniformly distributed throughout the images of the two remaining aerogel specimens, as would be expected if signal loss were due solely to xenon atom exchange. Moreover, entire regions which are devoid of signal intensity can be found in the two specimens at the center and left of Fig. 2D. Therefore, the amount of xenon adsorption varies significantly with spatial location in these two aerogels, and this suggests that their pore structures are heterogeneous in nature.

It should be pointed out that lower signal intensity seen in the image of the translucent specimen (middle) can be partly accounted for by T_2 weighting effects. The T_2 relaxation time of xenon inside this specimen is less than half that of the transparent samples. To better quantify this effect, we calculated the integrated signal intensity for 25 pixels near the center of the three aerogel images in Fig. 2A. The ratio of the average integrated signal intensities for the middle/right images was determined to be 0.50. The effect of T_2 weighting can be calculated using the expression

$$W = \exp[-\tau_E/T_2(52\,\text{ppm}))/\exp(-\tau_E/T_2(46\,\text{ppm})], \quad [2]$$

where $\tau_E = 3.8$ ms is the time to echo and the T_2 values are taken from Table 1. The T_2 weighting ratio, $W = 0.65$, was determined from the experimental data. The difference in T_2 values does not completely account for the entire reduction in signal intensity that is observed; therefore, we can conclude that less xenon is adsorbed in the middle specimen.

The results obtained thus far indicate that the pore structures in translucent and transparent specimens are fundamentally different. The shorter T_2 relaxation time of xenon in the translucent specimen (middle) is consistent with its having a more disordered pore network. Greater disorder would tend to induce nanoscopic magnetic field gradients at the interfacial regions of the walls that would enhance the relaxation rate due to bulk magnetic susceptibility anisotropy. The observation of a chemical shift to lower field is consistent with the average pore size being smaller for the translucent specimen.

Moreover, total absence of xenon at the edges of the specimen on the left (corresponding to translucent regions in Fig. 2D) suggests that entire regions of the pore network has been closed off to xenon gas. We surmise that this specimen has been physically damaged and may have been, at one time, more similar to the transparent specimen located at the right. On the other hand, the translucent specimen in the center has a characteristically different pore network to those of the other specimens, and its pore structure is likely to be a direct consequence of different processing conditions.

Bulk and Occluded Phase Xenon Atom Exchange

The selective chemical-shift imaging experiments afford us with the opportunity to investigate exchange of xenon atoms between the free gas and occluded aerogel phases. Germane to this is the issue that NMR images obtained through the application of the SECSI pulse sequence requires a finite period of time to select one of the ^{129}Xe spin reservoirs; the time period required is on the order of 1 s. The SECSI method of image filtering involves a selective population inversion of nuclear magnetization associated with one of the spin reservoirs, e.g., inversion of xenon spins in the bulk-gas phase. During the time scale of the SECSI experiment, the negatively (bulk-xenon phase) and positively (occluded phase) generated spin magnetizations admix via translational diffusion of xenon atoms between phases. Regions near the surface of the specimen tend to experience the greatest degree of mixing; consequently, positive spin magnetization in those regions should be diminished via exchange. The degree to which the image is modified depends directly on the magnetization exchange rate, the xenon T_1 relaxation rates, the geometry of the specimen, and the duration of the delay periods between pulses in the SESCI experiment.

In order to quantify the rate of the exchange, magnetization transfer experiments were carried out at room temperature on the high pressure sample, see Fig. 4. A 29% decrease in the signal intensity of occluded xenon was observed during the T_1–null evolution period in the SECSI experiment. This decrease in signal intensity can be accounted for by assuming a simple, single-atom transfer mechanism between xenon reservoirs.

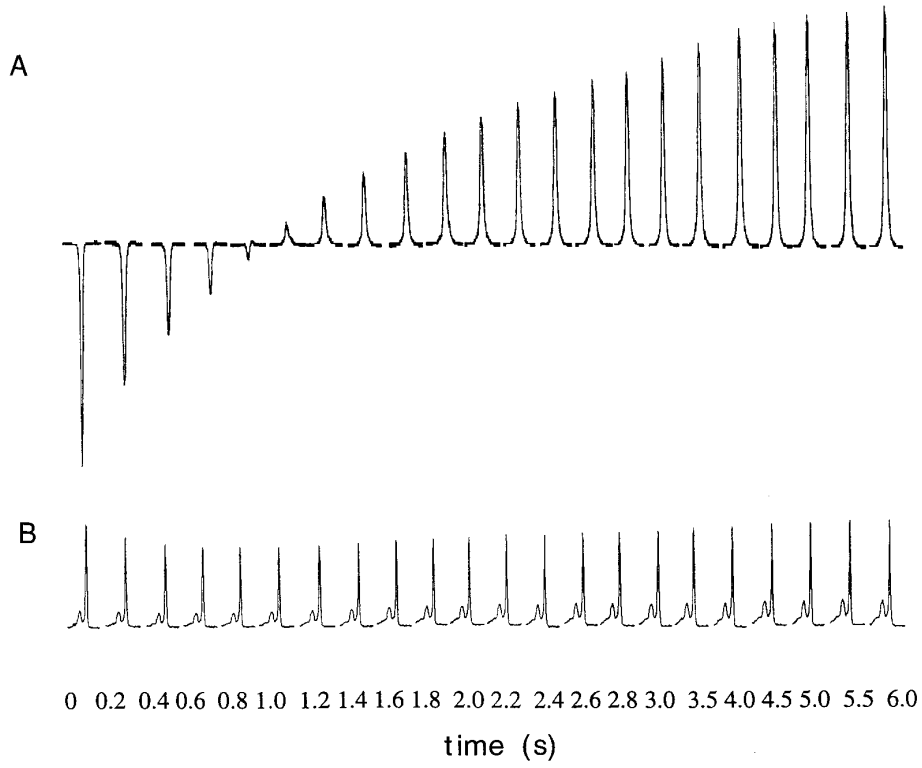

FIG. 4. Stacked plots of ^{129}Xe NMR spectra obtained from the magnetization exchange experiments on the high pressure sample. The resonance of the free gas (at 17 ppm) was inverted, and spectra were recorded after a variable delay period using a 90° readout pulse. Results for bulk-phase xenon are shown in (A) corresponding results for occluded xenon appear in (B).

Under this assumption, magnetization of the occluded phase is lost due to xenon atoms diffusing out of the aerogel specimens and, at the initial stages of the process, due to cancellation of positive magnetization from any inverted (negative) magnetization of bulk-phase xenon diffusing into the specimens. On the time scale of the imaging experiment, however, the net magnetization of the bulk-phase xenon reservoir has reached a null. Therefore, we estimate that approximately 29% of the xenon atoms within the aerogel specimens have been exchanged with bulk-phase xenon during the imaging experiment. The relative amount of the total magnetization that is exchanged will be sample dependent and, ultimately, will depend on both the size and shape of the aerogel specimens studied.

^{129}Xe NMR at Low Pressures

Separate NMR measurements were performed on silica aerogels at lower xenon pressures, in an attempt to understand the pressure dependence of the ^{129}Xe shifts. First, several translucent samples were selected and placed in a 10-mm NMR tube with 1500 Torr of xenon gas and 50 Torr of O_2. The ^{129}Xe NMR spectrum of this sample is shown in Fig. 5A and exhibits three distinct ^{129}Xe resonances. The most intense resonance at 0 ppm is due to free xenon gas; two weaker resonances at 45 and 22 ppm are also observed and are assigned to xenon that is occluded within the specimens. These latter two resonances suggest that two different pore structures are present, and may reflect the difference in the average size of the pores. To this sample, several transparent aerogel specimens were added, and the ^{129}Xe NMR spectrum was again recorded at a pressure of 1500 Torr of xenon and 50 Torr of O_2. The addition of transparent specimens resulted in the appearance of a new, sharper resonance at 34 ppm, as shown in Fig. 5B.

During the past decade, several authors have tried to correlate xenon chemical shifts with pore size and shape (*20–24*). Fraissard and co-workers (*22*) have studied several microporous zeolites and were able to find a simple relationship between the mean free path of a xenon atom inside a pore and the ^{129}Xe chemical shift extrapolated to zero pressure of xenon. In all cases, the xenon shift followed a linear relationship with xenon loading; the chemical shift was found to decrease with decreasing xenon pressure.

In a subsequent paper by the same group (*30*), it was shown that Fraissard's empirical relationship did not apply in the case of mesoporous aerosil samples. BET measurements indicated that the average pore sizes of these materials ranged from 15 to 30 nm, which would have resulted in a

xenon chemical shift of less than 10 ppm according to Fraissard's equation. Instead, the xenon shifts that were measured ranged from 40 to 90 ppm, and quite unexpectedly, the shifts were found to increase slightly with decreasing xenon pressure. The authors speculated that fast exchange between xenon atoms in aerosil mesopores and any larger crevasses formed between particles may have caused the anomalous results.

The xenon NMR results on silica aerogels are strikingly similar to the results found previously for aerosils. Figure 6 shows a plot depicting the variation of the ^{129}Xe chemical shift of the resonance at 34 ppm (xenon adsorbed in transparent specimens) with pressures from 100 to 1500 Torr. Low signal-to-noise of the broader, less intense resonances precluded measurement of accurate chemical-shift values at the lower xenon pressures. Although it is difficult at present to determine with certainty whether the exchange mechanism postulated by the Fraissard group is in any way operational in aerogels, BET isotherm measurements on our samples indicate that they exhibit a narrow pore-size distribution in the mesopore regime, with an average pore diameter of approximately 20 nm. Perhaps the general relationship of ^{129}Xe chemical shift to pore size is invalid for mesoporous systems. Unfortunately, given the limited range of sample preparation conditions investigated in the present study, it is difficult to assess all of the factors that are important in influencing the xenon chemical shifts in these materials. Future efforts will attempt to address these specific issues.

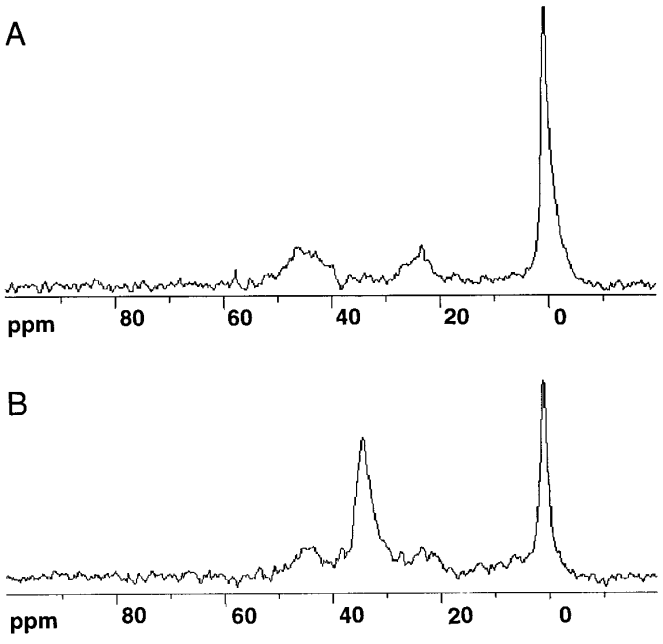

FIG. 5. (A) ^{129}Xe NMR spectrum of translucent aerogel specimens, which were placed in a 10-mm NMR tube to a height of 10 mm. The xenon pressure in the tube was 2 atm. (B) ^{129}Xe NMR spectrum of sample in which transparent aerogel specimens had been placed on top of translucent specimens, reaching an additional height of 10 mm; xenon gas pressure was 2 atm.

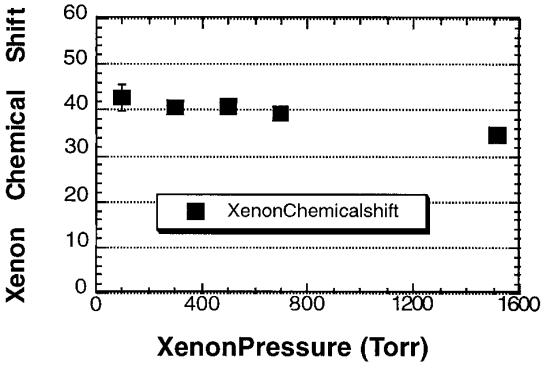

FIG. 6. Plot of ^{129}Xe chemical shift of occluded xenon in transparent aerogel specimens versus xenon pressure.

CONCLUSIONS

The use of ^{129}Xe NMR spectroscopic imaging has enabled the first direct observation of xenon occluded within a microporous material, and the method has been applied to the study of the pore structures of silica aerogels. Three different pore regions could be identified in the images of aerogels, and image contrast was correlated to the physical characteristics of the specimens. Optically transparent regions appeared in the images as areas of high xenon density, whereas translucent regions were correlated with areas of lower xenon density having different spectral characteristics, e.g., chemical shift and resonance linewidths. Areas devoid of xenon signal were identified in specimens from composite images depicting xenon in aerogels and the surrounding gas phase. These regions were correlated to a second type of translucency located near the edges of specimens and were ascribed to regions of extensive pore collapse caused by what may be physical damage to the specimens.

Bulk transport properties and gas diffusivities of bulk and occluded xenon phases were also measured. PFG diffusion measurements indicated diffusion of xenon to be anisotropic, but anisotropy was found only for pores having high optical transparency. The anisotropy may reflect an orientational alignment of the pore network as a result of processing conditions. Whether gravitational effects play a significant role in the orientational dependence of the pore network in aerogels will be the subject of future investigations. As an extension to the present studies, we also intend to make use of the pressure dependence of gaseous diffusion coefficients to derive mean free paths of molecular and atomic adsobates. From these measurements, we hope to obtain an estimate of the pore size and pore-size distributions in these systems.

From NMR magnetization transfer experiments on specimens with nominal volumes of 0.03 cm^3, we have estimated

that about 29% of the xenon atoms in aerogels were exchanged on the time scale necessary to perform the chemical-shift imaging experiment. Further study of xenon exchange phenomena under nonequilibrium conditions may illuminate the velocity and composition distribution profiles in flow of xenon near the surface of aerogels, and thus can in the future be used to better define mixing efficiencies responsible for gaseous diffusion processes in these systems.

ACKNOWLEDGMENTS

We thank Dr. David Noever for providing the aerogel samples and acknowledge partial support of this work from NASA, George C. Marshall Space Flight Center. We also express our appreciation to Joe Gregar for developing the techniques to prepare the high-pressure glass ampules used in this study. This work was performed under the auspices of the Office of Basic Energy Sciences, Division of Chemical Sciences, U.S. Department of Energy, under Contract W-31-109-ENG-38.

REFERENCES

1. G. Carlson, D. Lewes, K. McDinley, J. Richardson, and T. Tillotson, *J. Non-Cryst. Sol.* **186,** 372 (1995).
2. V. Wittwer, *J. Non-Cryst. Sol.* **145,** 233 (1992).
3. K. I. Jensen, *J. Non-Cryst. Sol.* **145,** 237 (1992).
4. S. Svendsen, *J. Non-Cryst. Sol.* **145,** 240 (1992).
5. M. Bourdinaud, J. B. Cheze, and J. C. Thevenin, *Nucl. Instrum. Meth.* **136,** 99 (1976).
6. A. J. Hunt and K. D. Lofftus, ''Process Considerations in Monolithic Aerogels'' (D. E. Clark, and D. R. Ulrich, Eds.), Better Ceramics Through Chemistry III, Vol. 121, p. 679, Materials Research Society, Pittsburgh (1988).
7. K. D. Lofftus, K. V. S. Shastri, and A. J. Hunt, *Proc. Adv. Mater. Soc. SME* **229 (1990).**
8. S. Brunauer, P. J. Emmett, and E. Teller, *J. Am. Chem. Soc.* **60,** 309 (1938).
9. S. J. Gregg and K. S. W. Sing, ''Adsorption, Surface Area and Porosity,'' Academic Press, London (1967).
10. S. Q. Zeng, A. J. Hunt, W. Cao, and R. Greif, *J. Heart Trans.* **116,** 756 (1994).
11. F. Ehrburger-Dolle, M. Holz, C. Mauzac, J. Lahaye, and G. M. Pajonk, *J. Non-Cryst. Sol.* **145,** 185 (1992).
12. G. W. Scherer, D. M. Smith, and D. Stein, *J. Non-Cryst. Sol.* **186,** 309 (1995).
13. G. Schuck and W. Dietrich, *in* ''Aerogels'' (J. Fricke, Ed.), p. 148, Springer-Verlag, Berlin (1986).
14. G. A. Nicolaon and S. J. Teichner, *Bull. Soc. Chim.* **9,** 3555 (1968).
15. G. W. Scherer, D. M. Smith, X. Qui, and J. M. Anderson, *J. Non-Cryst. Sol.* **186,** 316 (1995).
16. R. Pirard, S. Blaher, F. Brouers, and J. P. Pirard, *J. Mater. Res.* **10,** 2114 (1995).
17. E. Anglaret, A. Hasmy, E. Courtens, J. Pelous, and R. Vacher, *J. Non-Cryst. Sol.* **186,** 131 (1995).
18. P. J. Barrie and J. Klinowski, *Prog. NMR Spectr.* **24,** 91 (1992).
19. M. A. Springuel-Huet, J. L. Bonardet, A. Gedeon, and J. Fraissard, *Langmuir* **13,** 1229 (1997).
20. J. A. Ripmeester and C. I. Ratcliffe, *Anal. Chim. Acta* **283,** 1103 (1993).
21. J. A. Ripmeester, *J. Magn. Reson.* **56,** 247 (1982).
22. T. Ito and J. Fraissard, *J. Chem. Phys.* **76,** 5225 (1982).
23. J. Demarquay and J. Fraissard, *Chem. Phys. Lett.* **136,** 314 (1987).
24. B. F. Chmelka, R. Tyoo, S.-B. Liu, L. C. De Menorval, C. J. Radke, E. E. Petersen, and A. Pines, *J. Am. Chem. Soc.* **110,** 4465 (1988).
25. E. L. Hahn, *Phys. Rev.* **80,** 580 (1950).
26. R. L. Vold, J. S. Waugh, M. P. Klein, and D. E. Phelps, *J. Chem. Phys.* **48,** 3831 (1968).
27. A. J. Lucas, S. J. Gibbs, W. G. Jones, M. Peyron, J. A. Derbyshire, and L. D. Hall, *J. Magn. Reson. A* **104,** 273 (1993).
28. R. E. Gerald II, A. O. Krasavin, and R. E. Botto, *J. Magn. Reson. A* **123,** 1 (1996).
29. P. T. Callaghan, ''Principles of Nuclear Magnetic Resonance Microscopy,'' Clarendon Press, Oxford (1991).
30. W. C. Conner, E. L. Weist, J. Fraissard, T. Ito, Q. Chen, and M. A. Springuel-Huet, ''Int. Conf. Fundam. Adsorpt.'' (A. B. Mersmann and S. E. Scholl, Eds.), p. 977, AIChE, New York (1991).